A novel cathode flow field for PEMFC and its performance analysis

Zhuo Zhang, Fan Bai, Pu He, Zexi Li, Wen-Quan Tao[*]

Key Laboratory of Thermo-Fluid Science & Engineering of MOE, Xi'an Jiaotong University, Xi'an, Shaanxi 710049, PR China

HIGHLIGHTS

- A mass transfer enhanced novel flow field is proposed to improve cell performance.
- The power density of the novel flow field is increased by about 25.2% under 2.0 A/cm^2.
- A narrower C-D structure is more conducive to mass transfer and boosting performance.
- The droplet dynamic behavior proves better drainage capacity of novel flow field.

ARTICLE INFO

ABSTRACT

A good flow field design is important to the proton exchange membrane fuel cell (PEMFC) performance, especially under a high current density region, which is dominated by concentration polarization. Motivated by the variable cross-section channel idea, in this study, a novel flow field containing a converging-diverging (C-D) pattern is proposed. A three-dimensional multiphase model is established to study its performance. The numerical results show that it outperforms the conventional straight channel and only depth-variant channel. In the novel flow field the enhanced under land cross flow and higher effective mass transfer coefficient both improve the reactant transport. The effects of operating conditions, like stoichiometric ratio and operating pressure, on cell output performance are studied. It is found that a higher promotion rate can be obtained by increasing the stoichiometric ratio, but increasing the operating pressure has little effect. The droplet dynamic behavior in the C-D channel and straight channel are studied, and the results prove the better drainage capability of the novel flow field.

© 2023 Hydrogen Energy Publications LLC. Published by Elsevier Ltd. All rights reserved.

Introduction

Under the dual pressure of environmental protection and energy crisis, the PEMFC has become the research hotspot with the advantage features like high power density, high energy conversion efficiency, fast dynamic response, zero-emission, etc [1]. Among the components, the flow field plate (FFP) or bipolar plate (BP) contributes the second biggest part of the whole PEMFC stack system cost [2]. It plays an important role in the PEMFC stack. The main functions of BP consist of (i)electric current collection; (ii)water and heat removal; (iii)gaseous reactant distribution; (iv)mechanical support; (v) the anode and cathode reactants isolation. The above functions put forward many requirements for the

---

Nomenclature

A_{act}	active area(m^2)
A_{in}	inlet area(m^2)
c	concentration(mol/m^3)
C_l	volume fraction(J/(kg·K))
C_p	specific heat capacity(J/(kg·K))
D	diffusivity(m^2/s)
EW	equivalent molecular weight of dry membrane (kg/kmol)
F	Faraday's constant(96,485 C/mol)
h	height(m)
I	current density(A/m^2)
j	reaction velocity(A/m^3)
K	permeability(m^2)
k	thermal conductivity(W/(m·K)) or interface curvature
l	length
M	molar mass(kg/kmol)
n_d	electroosmotic drag coefficient
p	pressure(Pa)
q_v	volume flow rate(m^3/s)
R	gas constant (J/(mol·K))
RH	relative humidity
S	source term
s_{lq}	liquid saturation
T	temperature(K)
$\vec{u}$	velocity(m/s)
W_{pump}	pumping loss
w	width or through-plane velocity
Y	mass fraction

Greek letters

ε	porosity
α	transfer coefficient
σ	surface tension coefficient(N m^{-1})
δ	thickness(m)
ρ	density(kg/m^3)
μ	dynamic viscosity (Pa·s)
κ	electrical conductivity (S/m)
γ', γ	phase change rate(1/s)
ξ	stoichiometry ratio
ς	compressor efficiency
η	over potential (V)
ϕ	potential(V)
ϕ	solving varible
λ	membrane water content
ΔS	entropy production (J/(kmol·K))

Subscripts and superscripts

a	anode
act	activation
BP,FFP	bipolar plate
c	cathode
CL	catalyst layer
eff	effective value
ele	electronic
eq	equilibrium water content
g	gas
i	certain gas species
ion	proton
l,lq	liquid water
lh	latent heat
mw	membrane water
mem	membrane
sat	saturation
v-l	vapor to liquid
v-m	vapor to membrane water (vice verse)
vp	water vapor

material properties of BP, such as good corrosion resistance, good electrical conductivity, low cost, light weight, high mechanical strength, low gas transmittance, etc [3,4]. According to the material category, the existing commercial BPs could be divided into metal BPs and graphite-polymer composite BPs. For both kinds of BPs, from material selection, surface modification, to manufacturing and property test, many fundamental studies have been done [5—10]. In addition to the material problems, another critical issue of BPs is about flow field design, or BP's geometry design [11—13].

It is well known that parallel, serpentine, interdigitated, and their combination flow field are widely used in commercial PEMFC bipolar plates. To further improve the performance, much work has been done based on these basic designs. One common way is to adjust the flow pattern. Xu et al. [14] proposed a convection-enhanced serpentine flow field, which was obtained by re-patterning conventional single serpentine flow fields. The application of this new flow field to the fuel cell resulted in a substantial performance increase in the mass-transport limitation region as compared with the conventional flow field. Zhang et al. [15] investigated

the serpentine flow field PEMFC performance under the effect of channel length and channel width-depth combinations. The results show that the 8-channel complex flow field is the best channel pattern. Min et al. [16] numerically studied a serially-linked serpentine flow field for PEMFC. The effect of the segment number and channel path number on the cell performance was analyzed. The results showed that the cell performances could be improved by increasing the segment number or the channel path number in each segment. Xu et al. [17] experimentally and numerically investigated the effect of the cathode flow field opening shape, cathode endplate thickness, cathode flow field open ratio, and orientation on the performance of the air-breathing high temperature PEMFC. Shimpalee et al. [18] investigated how 200 cm^2 serpentine flow fields with a different number of gas paths, and thus different gas path lengths, affect performance and species distribution. It was found that the shorter path length gives a more uniform current density distribution and less condensed liquid water than the longer path. Limjeerajarus et al. [19] adjusted the number of gas inlets and outlets on a hybrid serpentine-interdigitated flow field and achieved

performance improvement and a much more uniform distribution of key physical quantity. Hazar et al. [20] used main collector channels to restrict the uneven distribution of reactants in parallel intermediate channels. The study revealed that the geometric dimensions of the flow channels had a substantial impact on the chemical reactions and electrical characteristics of the cell. Based on parallel flow field, Zhang et al. [21] designed and simulated the performance of a waveform flow field. The index "gas concentration error" showed that the uniformity of this flow field is better than traditional flow fields. Similarly, Rahmani et al. [22] presented a new wavyflow field with various waviness parameters. The results showed that increasing the amplitude or increasing the wavelength is helpful for improvement of output performance.

The bionic method has been explored to date widely, and it is gradually applied in the PEMFC flow field design [23]. Sauermoser et al. [24] conducted an experimental analysis of width scaling parameters in tree-like flow field plates. A reduction of the number of branching generation levels and width scaling factor were recommended by the authors. The nature-spired flow channel design following Murray's law of branching was manufactured by Kahraman and Coban [25] and demonstrated a higher performance compared with the typical serpentine design. Trogadas et al. [26] introduced a lung-inspired fractal flow field to overcome reactant homogeneity issues in PEMFC. And uniformity in reactant distribution and minimal pressure drop were retained during scale-up, demonstrating the robustness of the proposed nature-inspired approach across length scales.

As a major milestone in PEM fuel cell commercialization, in 2014, Toyota released its first generation of fuel cell vehicles (FCV), MIRAI. In its fuel cell system, a 3D fine mesh flow field was developed. Unlike above mentioned 2D flow fields, the 3D flow field can promote gas transport to the cathode catalyst layer and quickly draw out the generated water [27]. Therefore, the 3D flow field has attracted more and more attention. Cai et al. [28] and Shen et al. [29] presented a 3D flow field consisting of transport enhanced main channel, sub-channel, and transition areas. The simulation results showed the 3D flow field could enhance the mass transfer ability and improve the PEMFC performance. Chen et al. [30] proposed a 3D wave flow channel to enhance the mass transfer and current density. The optimal flow channel minimum depth and wave length were determined. Furthermore, Yan et al. [31] designed a 3D gradient waved channel to increase flow velocity at both in-plane and through-plane directions along the channel length. Porous type flow field has showed great promises in enhancing reactant supply, heat removal and electrical conduction, reducing the concentration performance loss and improving operational stability for fuel cells [32]. Metal foam materials with high porosity (>90%) have also been proposed as alternative flow fields for PEM fuel cells [33]. Zhang et al. [34] reconstructed the metal form flow field and adopted the 3D multiphase model to study the cell performance. The results showed that the metal foam flow field increases fuel cell performance under high current density compared with the conventional channel-rib flow field. Bao et al. [35,36] used the
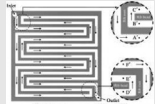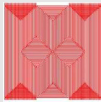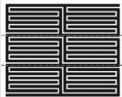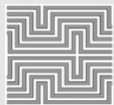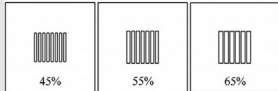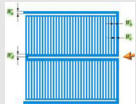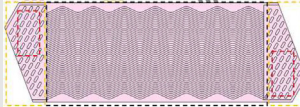
volume of fluid (VOF) method to investigated liquid droplet removal and dispersion in metal form flow field. In their study, the full morphology of metal foam is reconstructed through the X-ray computational tomography. Azarafza et al. [37] performed a comparative study of several types of cathode flow field designs. The parametric analysis reveals that the metal foam outperforms other designs at intermediate and high humidity conditions.
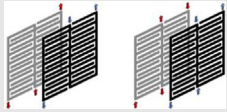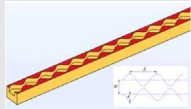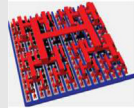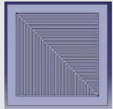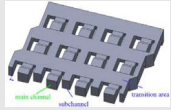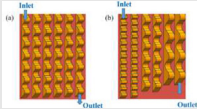
Besides, baffled flow channels are also widely studied 3D channels that can promote mass transfer effectively [38]. Perng et al. [39] inserted rectangular obstacles into a straight or narrowed flow channel. Better gas reactant transport and local cell performance are produced near the obstacles. Wang et al. [40] proposed a novel dot matrix and sloping baffle flow field plate, which consists of dispersive and arrayed blocks with sloping angles as shoulders. It could achieve high cell output performance by both improving oxygen supply to the gas diffusion layer (GDL) and uniform distribution. Niu et al. [41] and Fan et al. [42] inserted an air baffle, lateral water baffle, and middle water baffle into the flow channel and achieved 7% improvement of performance under high operating current density compared with the conventional empty flow channel. The effect of geometry parameters on PEMFC performance is investigated. Heidary et al. [43] experimentally investigated the effect of in-line and staggered blockage configurations within a parallel flow field and compared results with those of a baseline parallel flow field without blockage. The author suggested that the staggered blockages are a promising design for the PEMFC flow field. Guo et al. [44] studied the effect of the baffle shape and developed a baffled flow channel with optimized windward side and leeward side. The power loss accounted by the pumping power in the reactant delivering process was reduced, and the cell performance was further improved. Ghanbarian and Kermani [45] studied the channel indentation in high current density and carried out a parameterized analysis of dent heights and arrangement. It was observed that in the regions right above the dents, the local current density was crowned. Cai et al. [46] discussed the influence of cross-section shapes of blockages and dimensionless blockage length on cell performance. The flow-guide part and the suppression part need to exisit at the same time to enhance the mass transfer.

3D flow field design has become a promising alternative for PEMFC, but a few issues remain with this approach. Zhang et al. [47] found that the 3D fine mesh flow field is not favorable to the PEMFC operating under the ohmic dominated region due to the fact that the decreased contact area between GDL may increase the ohmic loss. What's more, the existence of these baffles made the manufacturing process of the flow field challenging and expensive because of the complex structure of baffles which leads to difficulties in the machining process.

Variable cross-section channels, which is between 2D and 3D flow field, could become the best promise to easy fabrication and mass transfer enhancement. Rezaie et al. [48] and Havaej [49] designed a flow field comprised of converging and diverging channels (neighboring channels). Havaej [49] found that there was a gradient pressure from the converging
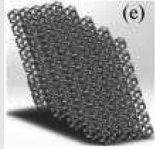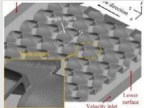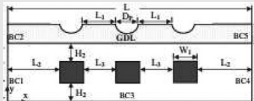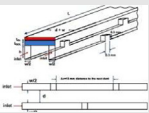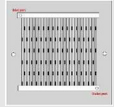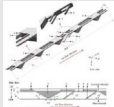
Table 1 – Review of selected past studies with various flow field designs.
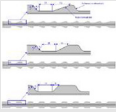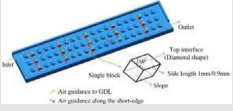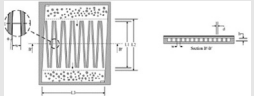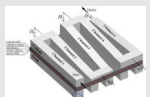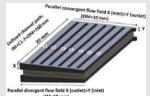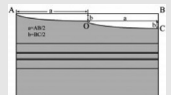
Authors (Year)	Flow field type	Features	Schematic	Reference
Xu et al. (2006)	Serpentine	Convection-enhanced serpentine flow field		[14]
Shimpalee et al. (2006)	Serpentine	Path lengh and paatern		[18]
Min et al. (2019)	Serpentine	Modified serially—linked serpentine flow fields		[16]
Zhang et al. (2021)	Serpentine	8-channel complex serpentine flow field		[15]
Xu et al. (2019)	Parallel	Opening shape/open ratio		[17]
Hazar et al. (2022)	Parallel	Main collector channels		[20]
Zhang et al. (2022)	Parallel	Complex waveform staggered flow field		[21]

Limjeerajarus et al. (2020)	Hybrid serpentine-interdigitated flow field	Modification of the number of gas inlets/outlets		[19]
Rahmani et al. (2023)	2D wave	Raccoon channel		[22]
Trogades et al. (2018)	Biomimetic	Lung-inspired fractal flow field		[26]
Kahraman et al. (2020)	Biomimetic	Natural-inspired flow fields		[25]
Sauermoser et al. (2021)	Biomimetic	Tree-like flow fields with different design rules		[24]
Cai et al. (2018) and Shen et al. (2020)	Novel 3D structure	Consisting of transport-enhanced main channel, sub-channel, and transition areas.		[28,29]
Yan et al. (2019) and Chen et al. (2020)	3D wave	Optimize the channel the minimum depth and wave length		[30,31]

Table 1 – (continued)				
Authors (Year)	Flow field type	Features	Schematic	Reference
Zhang et al. (2020)	Metal foam	Full morphology of a metal foam material		[34]
Bao et al. (2020)	3D fine mesh	The single- and two-phase flow characteristics		[36]
Perng et al. (2014)	Baffled	Rectangular obstacles inserted		[39]
Ghanbarian et al. (2016)	Baffled	Zigzag dent arrangement		[45]
Heidary et al. (2016)	Baffled	Staggered blockage configurations		[43]
Niu et al. (2018) and Fan et al. (2018)	Baffled	Multi-plates structure channel and integrated structure channel		[41,42]

Guo et al. (2019)	Baffled	Baffled flow field with optimized windward side and leeward side		[44]
Wang et al. (2019)	Baffled	Dot matrix and sloping baffle flow field		[40]
Razaie. (2017) and Havaej et al. (2019)	Varying the channel width	Converging and diverging channels (neighboring channels)		[48,49]
Ramin et al. (2019)	Varying the channel width	Trap-shape channels		[53]
Wang et al. (2010)	Varying the channel depth	Serpentine flow field with changing channel height		[51]
Timurkutluk et al. (2018)	Varying the channel depth	Converging or diverging channels		[50]
Song et al. (2019)	Varying the channel depth	Nonuniform depth channel of different shape		[52]

Fig. 1 – Review of flow field design (Refer to Table 1 for picture source).

(a) Novel flow field plate

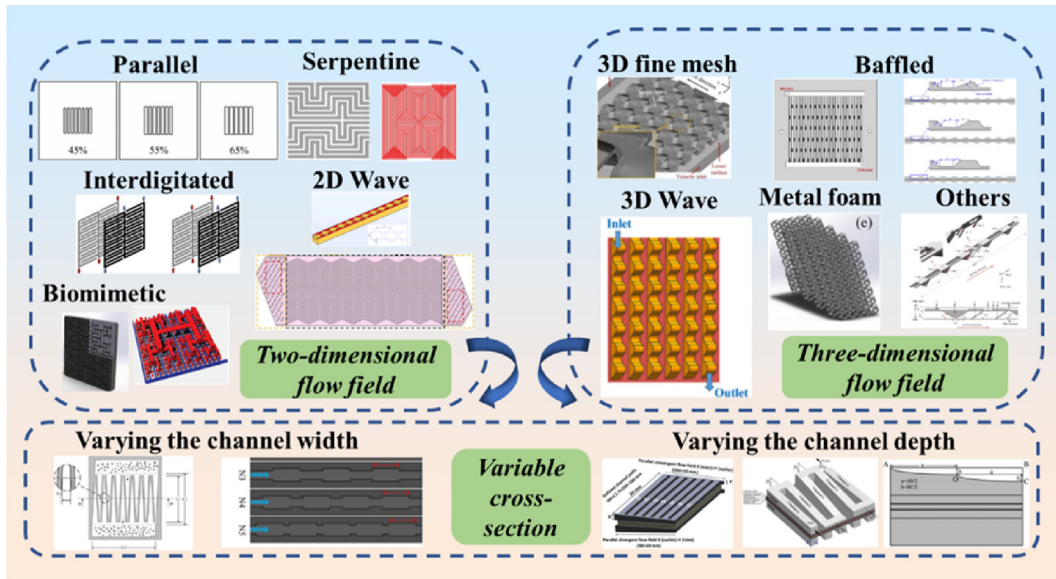(b) Conventional flow field plate
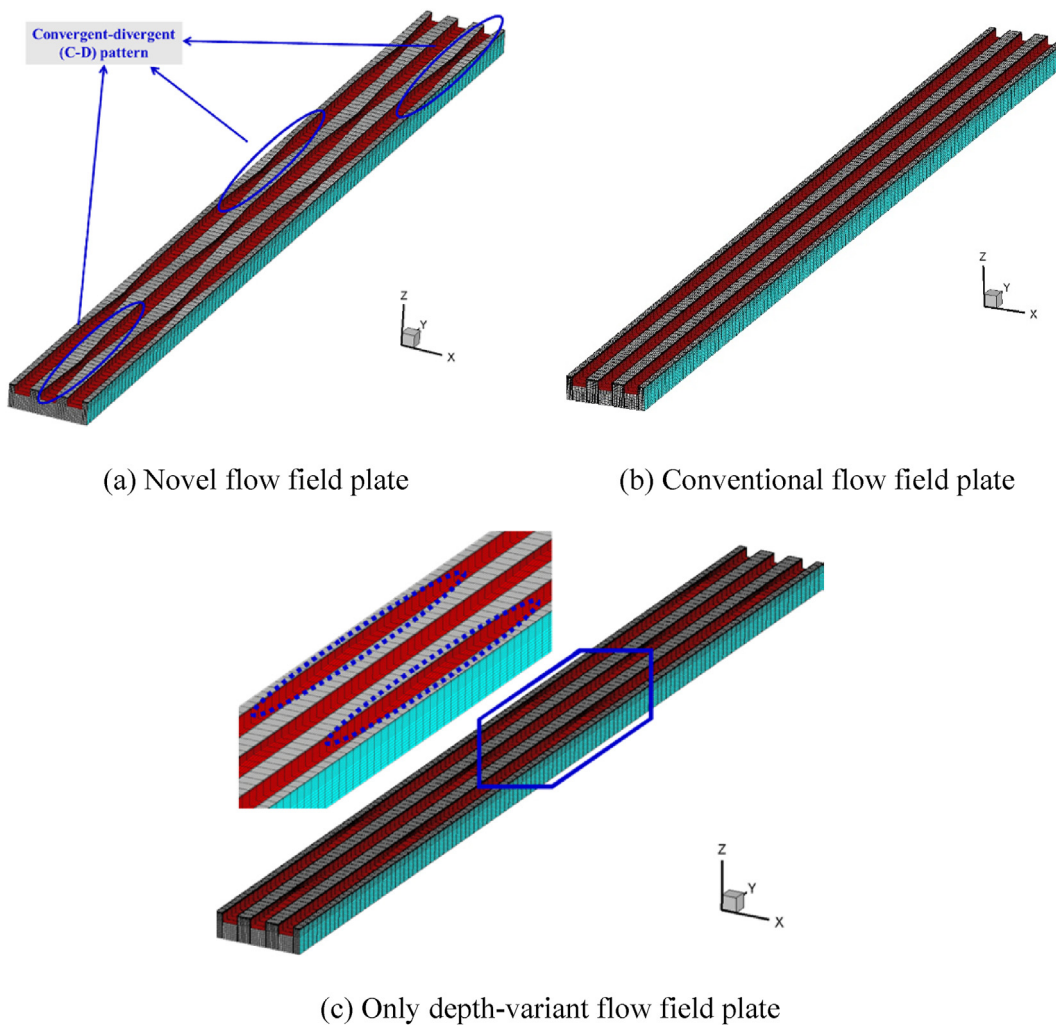

(c) Only depth-variant flow field plate

Fig. 2 – Novel and straight flow field plate.

channel towards its nearby diverging channel. The polarization curves show that by applying an angle of 0.3° to the channels, the net electrical output power increases by 16% compared with the straight base case [48]. Timurkutluk et al. [50] modified the classical parallel flow channel by varying the channel depth with different constant inclination gradients from inlet to outlet and achieved a maximum 16% improvement of cell power density. Wang et al. [51] used a special optimization approach to optimize the channel heights of a cathode single serpentine flow field with five channels. The optimal channel design has three tapered channels (channels 2−4) and one diverging channel (channel 5). Song et al. [52] compared the cell performance of nonuniform depth and conventional straight channels in a unitized regenerative fuel cell (URFC). In fuel cell mode, when the average channel depth is the same, the net power of the straight channel is always lower than the nonuniform depth case. Ramin et al. [53] proposed a trap-shaped channel design having narrower lands at a number of cross-sections. There existed optimal length and number of traps which substantially enhanced the PEMFC performance. A review of selected past studies is presented in Table 1. In general, the flow field design mentioned above can be classified as two-dimensional (2D), three-dimensional (3D) flow field and variable cross-section flow field. To provide a clear and comprehensive picture of the state of the art, a schematic diagram is shown in Fig. 1.

It can be seen that the width and depth variation is beneficial for the PEMFC performance. Learning from this idea, the convergent-divergent structure at a local position in parallel channels is introduced and a novel flow field is proposed. The difference between our converging-diverging flow field and the ones mentioned in the above review are as follows. Firstly, in the convergent or divergent channel in existing literature, the cross-sectional are simply monotonically changed rather than arranged regularly and periodically, as designed in this paper. Secondly, different from 3D wave [30,31], baffled [39,40], and trap-shape channels [53], the depth and width of the channel designed in this paper change simultaneously and continuously. And this configuration is staggered between adjacent flow channels. The objective is to improve mass transport and decrease concentration loss under high current density. The designed new flow field has the

Table 2 − Geometry parameters.		
Parameters	Symbol	Value
Novel flow field		
Length of C-D part (mm)	l_1	10
Length of the straight part (mm)	l_2	10
Width of C-D part (mm)	w_1	0.5
Width of straight part (mm)	w_2	1.0
Depth of C-D part (mm)	h_1	0.275
Depth of straight part (mm)	h_2	0.55
Width of rib	w_3	0.7
3D multiphase model		
Total length (mm)	l_0	60
Total width (mm)	w_0	5.1
Thickness of GDL (μm)	δ_{GDL}	130
Thickness of MPL (μm)	δ_{MPL}	45
Thickness of CL (μm)	$\delta_{ACL}/\delta_{CCL}$	6/18 (anode/cathode)
Thickness of PEM (μm)	δ_{PEM}	15
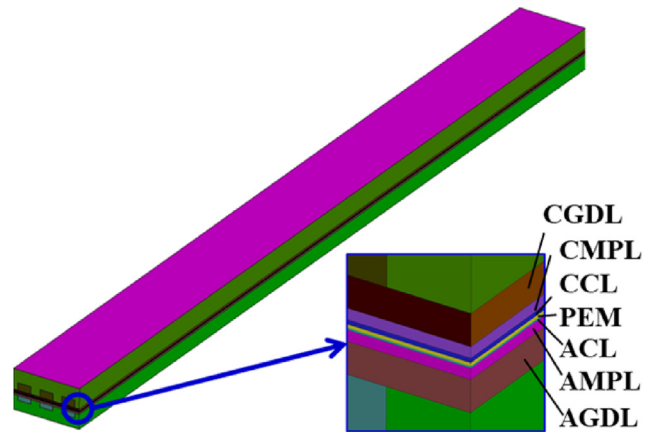
Fig. 4 − Computational domain for 3D multiphase model.

advantages of simple structure, easy processing, high output performance, and fast drainage speed.

Then three-dimensional multiphase model is adopted to simulate the cell performance with different flow fields. Furthermore, for novel flow fields, the effect of operating
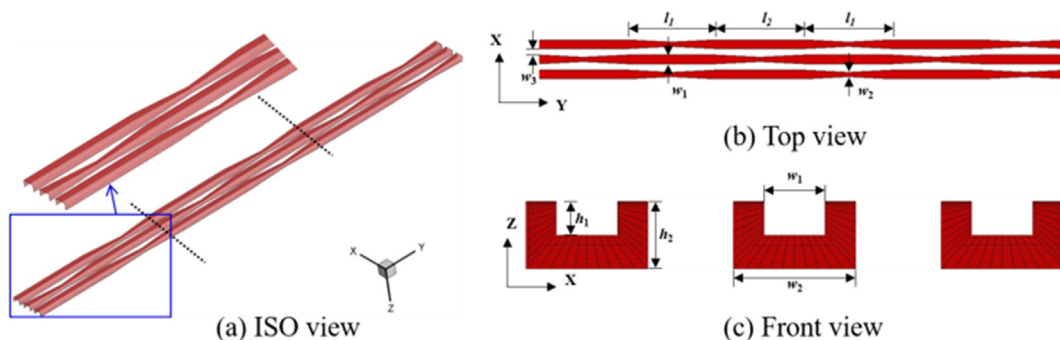
Fig. 3 − Novel flow field.

Table 3 – Source terms.

Source terms	Unit
Mass conservation equation: $S_m = S_{H_2} + S_{O_2} + S_{vp}$ (all zones)	kg/(m^3·s)
Momentum conservation equation: $S_u = \begin{cases} -\dfrac{\mu_g}{K_g}\vec{u}_g \ (\text{CLs}, \text{GDLs and GDLs}) \\ 0 \ (\text{other zones}) \end{cases}$	kg/(m^2·s^2)
H$_2$ conservation equation: $S_{H_2} = \begin{cases} -\dfrac{j_a}{2F}M_{H_2} \ (\text{anode CL}) \\ 0 \ (\text{other zones}) \end{cases}$	kg/(m^3·s)
O$_2$ conservation equation: $S_{O_2} = \begin{cases} -\dfrac{j_c}{4F}M_{O_2} \ (\text{cathode CL}) \\ 0 \ (\text{other zones}) \end{cases}$	kg/(m^3·s)
Water vapor conservation equation: $S_{vp} = \begin{cases} -S_{v-l} + S_{v-m}M_{H_2O} \ (\text{CLs}) \\ -S_{v-l} \ (\text{MPLs}, \text{GDLs}) \\ 0 \ (\text{other zones}) \end{cases}$	kg/(m^3·s)
Condensation/evaporation: $S_{v-l} = \begin{cases} \gamma\varepsilon(1-s_{lq})(\rho_{vap}-\rho_{sat}), \rho_{vap} > \rho_{sat} \\ \gamma\varepsilon s_{lq}(\rho_{vap}-\rho_{sat}), \rho_{vap} < \rho_{sat} \end{cases}$	kg/(m^3·s)
Electrons conservation equation: $S_{ele} = \begin{cases} -j_a \ (\text{anode CL}) \\ j_c \ (\text{cathode CL}) \\ 0 \ (\text{other zones}) \end{cases}$	A/m^3
Protons conservation equation: $S_{ion} = \begin{cases} j_a \ (\text{anode CL}) \\ -j_c \ (\text{cathode CL}) \\ 0 \ (\text{other zones}) \end{cases}$	A/m^3
Liquid pressure conservation equation: $S_{lq} = \begin{cases} S_{v-l} \ (\text{anode CL}, \text{MPLs}, \text{GDLs}) \\ \dfrac{j_c}{2F}M_{H_2O} + S_{v-l} \ (\text{cathode CL}) \\ 0 \ (\text{other zones}) \end{cases}$	kg/(m^3·s)
Membrane absorption and desorption: $S_{v-m} = \dfrac{\rho_m}{EW}(\lambda_{mw} - \lambda_{eq})\gamma'$	mol/(m^3·s)
Dissolved water conservation equation: $S_{mw} = \begin{cases} -S_{v-m} - \rho_{lq}\dfrac{K_{MEM}}{M_{H_2O}\mu_{lq}}\dfrac{p_{lq}^{\overline{ACL}} - p_{lq}^{\overline{CCL}}}{\delta_{MEM}\delta_{ACL}} \ (\text{anode CL}) \\ 0 \ (\text{other zones}) \\ -S_{v-m} + \rho_{lq}\dfrac{K_{MEM}}{M_{H_2O}\mu_{lq}}\dfrac{p_{lq}^{\overline{ACL}} - p_{lq}^{\overline{CCL}}}{\delta_{MEM}\delta_{CCL}} \ (\text{cathode CL}) \end{cases}$	mol/(m^3·s)
Energy conservation equation: $S_E = \begin{cases} j_a|\eta_{act}| + \|\nabla\phi_{ele}\|^2\kappa_{ele}^{eff} + \|\nabla\phi_{ion}\|^2\kappa_{ion}^{eff} + S_{lh} \ (\text{anode CL}) \\ \dfrac{j_cT\Delta S}{4F} + j_c|\eta_{act}| + \|\nabla\phi_{ele}\|^2\kappa_{ele}^{eff} + \|\nabla\phi_{ion}\|^2\kappa_{ion}^{eff} + S_{lh} \ (\text{cathode CL}) \\ \|\nabla\phi_{ele}\|^2\kappa_{ele}^{eff} + S_{lh} \ (\text{GDL}, \text{MPL}) \\ \|\nabla\phi_{ele}\|^2\kappa_{ele}^{eff} \ (\text{BP}) \\ \|\nabla\phi_{ion}\|^2\kappa_{ion}^{eff} \ (\text{membrane}) \\ 0 \ (\text{other zones}) \end{cases}$	W/m^3

conditions and geometry parameters on performance are numerically investigated. Besides, the drainage performance of the novel and conventional channels is compared using the VOF method. The rest of the paper is organized as follows. The characteristics of the proposed novel flow field structure and numerical model are introduced in Section 2. The detailed results and discussion are presented in Section 3. Lastly, the main conclusions are summarized in Section 4.

Model description

In this section, the structure of the novel flow field is displayed in Section 2.1. Then the three-dimensional multiphase model (Sections 2.2 and 2.3) and VOF model (Section 2.4) adopted are illustrated. The respective model assumptions are also described in the corresponding

chapters. Furthermore, Section 2.5 introduce an index to evaluate the mass transfer ability. Finally, the numerical procedure is given in Section 2.6.

Novel flow field design

The novel flow field plate proposed is shown in Fig. 2(a), and the conventional straight and only depth-variant flow field plates are also shown in Fig. 2(b) and (c), respectively, for comparison. The convergent-divergent (C-D) pattern is introduced periodically in the novel flow field plate, while the cross-sectional area along the flow direction remains unchanged in the straight flow field plate. Different from the novel flow field plate, the change of the cross-sectional area of the depth-variant channel is only caused by the depth variation.

As shown in Fig. 3(a), the novel flow field could be regarded as obtained by the translation of repeated units. The black dotted line in Fig. 3(a) splits the flow field according to the repeated unit. A repeated unit consists of a straight part and a C-D part. The C-D pattern is staggered arranged between two adjacent channels, which ensures both straight and C-D parts are misaligned between adjacent channels.

The related dimension of the novel flow field is annotated in Fig. 3 (b) (top view) and Fig. 3 (c) (front view). The values are listed in Table 2. It is worth emphasizing that the width (from w_1 to w_2) and depth (from h_1 to h_2) of the channel both change linearly at C-D locations. This feature is considerably crucial in terms of feasibility and low cost of the fabrication of the bipolar plates, especially when it comes to mass production. In addition, the channel wall of the novel flow field is treated with a hydrophilic coating which is beneficial for absorbing droplets.

Computational domain

Fig. 4 shows the computational domain in the performance simulation. It consists of BP, GC (or flow field), GDL, microporous layer (MPL), and catalyst layer (CL) in both the anode and cathode sides. And a proton exchange membrane (PEM) zone is sandwiched in anode and cathode. The related dimensions are listed in Table 2. The kinetic process of oxygen reduction reaction (ORR) on the cathode is extremely slow, which is the control step of the overall reaction. Moreover, at high electrical density, the cathodic half-reaction is more critical, due to the oxygen diffusivity is much lower than hydrogen diffusivity. Therefore, the novel flow field proposed is only adopted in the cathode, while the straight channel is always on the anode side. Both anode and cathode flow fields are made of 3 parallel channels.

3D two-fluid model

Governing equations

The 3D two-fluid model is adopted to simulate the cell performance. Some assumptions are made as follows.

(1) The fuel cell runs under a steady condition;
(2) The flow is laminar; Both the gas species and the gas mixture follow the ideal gas law;
(3) The high gas velocity in the channel could blow out the liquid water completely. This assuption is widely adopted and also based on our own pratice. According to our previous research experience [3], in the commercial PEMFC, during normal operation, the liquid water in the gas channel area can be quickly carried away by the air flow, and only in the case of water flooding or other failures will water accumulate in the local part of the channel. In addition, the computational domain in this paper is a short straight (no turning) channel. As a result, the amount of liquid water in channels is fixed as zero [54–56].
(4) The contact resistance between different layers is ignored, which is employed in many modeling works.
(5) The coolant channel is simplified to a thermal convection condition, considering the small active area of the computational domain [22,57,58].

Mass conservation equation (solved in GCs, GDLs, MPLs, CLs):

$$\nabla \cdot \left(\rho_g \vec{u}_g \right) = S_m \tag{1}$$

Momentum conservation equation (solved in GCs, GDLs, MPLs, CLs):

| Table 4 – Material property and operating condition.			
Parameters	Value	Unit	Ref
Density of MEM	1980	kg/m^3	[59]
Equivalent weight of MEM	1100	kg/kmol	[59]
Porosities of GDL; MPL; CL	0.6; 0.4; 0.3		[59,60]
Contact angles of GDL; MPL; CL	110; 120; 95	°	[47]
Intrinsic permeabilities of GDL; MPL; CL	$2.0 \times 10^{-12}/1.0 \times 10^{-12}/1.0 \times 10^{-13}$	m^2	[59]
Electrical conductivities of GDL; MPL; CL; BP	6000/5000/5000/20,000	S/m	[40,47]
Thermal conductivities of GDL; MPL; CL; MEM; BP	0.585; 0.27; 0.27; 0.109; 129	W/(m·K)	[3]
Specific heat capacities of GDL; MPL; CL; MEM; BP	861; 800; 240; 1287; 710	J/(kg·K)	[3]
Operating temperature	353.15	K	[59]
Operating pressure (anode/cathode)	50/50	kPa	
Stoichiometric ratio (anode/cathode)	1.5/1.5		
Relative humidity	100%/100%		[59]
Reference exchange current density	$3.0 \times 10^7/30.0$	A/m^3	[59]
Reference H$_2$/O$_2$ concentration	56.4/40.0	mol/m^3	[59]
Transfer coefficient	0.5/1.0		[59]

(a) Straight channel

(b) C-D channel
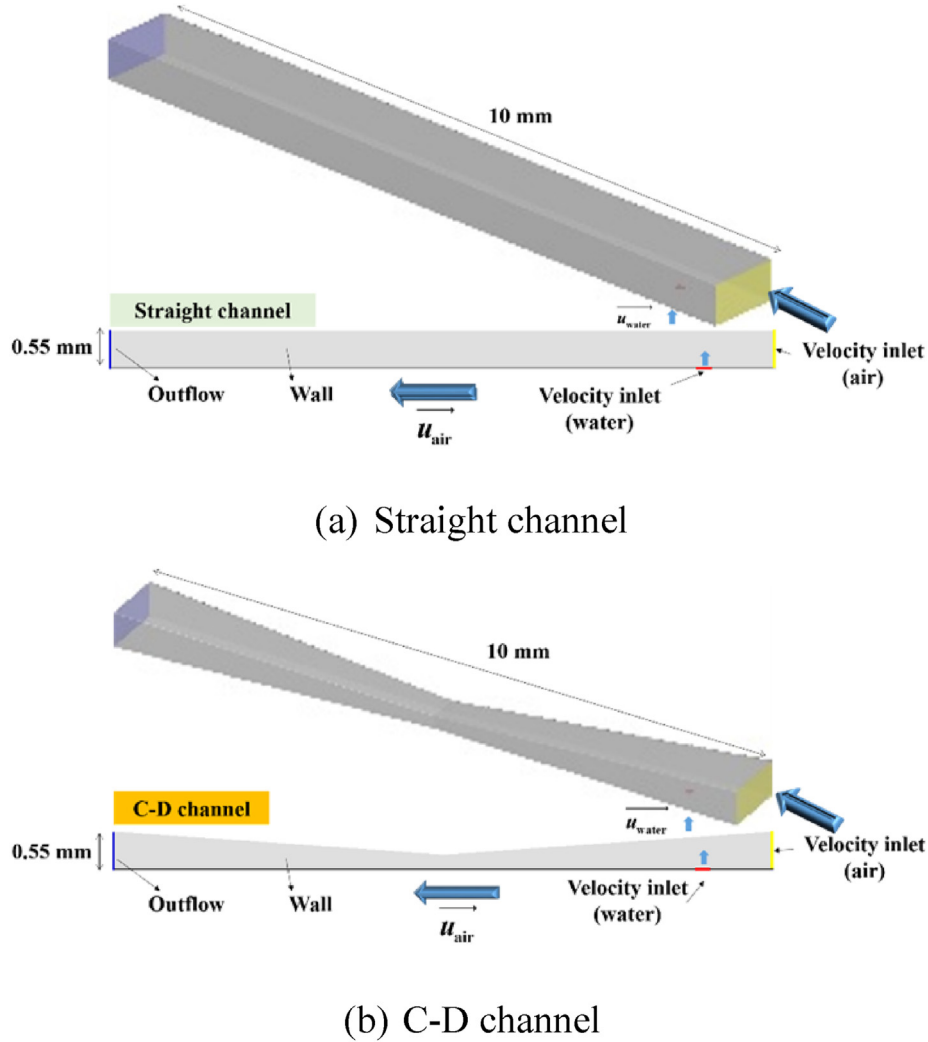
Fig. 5 — Computational domain of water transport.

$$\nabla \cdot \left(\frac{\rho_g \vec{u}_g \vec{u}_g}{\varepsilon^2 \left(1 - s_{lq}\right)^2} \right) = -\nabla p_g + \mu_g \nabla \cdot \left(\nabla \left(\frac{\vec{u}_g}{\varepsilon \left(1 - s_{lq}\right)} \right) + \nabla \left(\frac{\vec{u}_g^T}{\varepsilon \left(1 - s_{lq}\right)} \right) \right)$$
$$- \frac{2}{3} \mu_g \nabla \left(\nabla \cdot \left(\frac{\vec{u}_g}{\varepsilon \left(1 - s_{lq}\right)} \right) \right) + S_u$$

$$(2)$$

Species conservation equation of i-species (solved in GCs, GDLs, MPLs, CLs): (i: H_2, O_2, water vapor)

$$\nabla \cdot \left(\rho_g \vec{u}_g Y_i \right) = \nabla \cdot \left(\rho_g D_i^{eff} \nabla Y_i \right) + S_i \qquad (3)$$

Electrons conservation equation (solved in BPs, GDLs, MPLs, CLs):

$$0 = \nabla \cdot \left(\kappa_{ele}^{eff} \nabla \phi_{ele} \right) + S_{ele} \qquad (4)$$

Protons conservation equation (solved in MEM, CLs):

$$0 = \nabla \cdot \left(\kappa_{ion}^{eff} \nabla \phi_{ion} \right) + S_{ion} \qquad (5)$$

Liquid pressure conservation equation (solved in GDLs, MPLs, CLs):

$$0 = \nabla \cdot \left(\rho_l \frac{K k_{lq}}{\mu_{lq}} \nabla p_{lq} \right) + S_{lq} \qquad (6)$$

Dissolved water conservation equation (solved in MEM, CLs):

$$\nabla \cdot \left(\frac{n_d}{F} \nabla I_{ion} \right) = \frac{\rho_{mem}}{EW} \nabla \cdot \left(D_{mw}^{eff} \nabla \lambda_{mw} \right) + S_{mw} \qquad (7)$$

Energy conservation equation (solved in the whole domain):

Table 5 — Boundary conditions of water transport model.

Parameters	Value	Unit
Inlet air velocity	3.0	m/s
Inlet water velocity [64]	0.1	m/s
Contact angle of GDL [65]	140	°
Contact angle of GC [65]	60	°
Surface tension coefficient [64]	0.0725	N/m
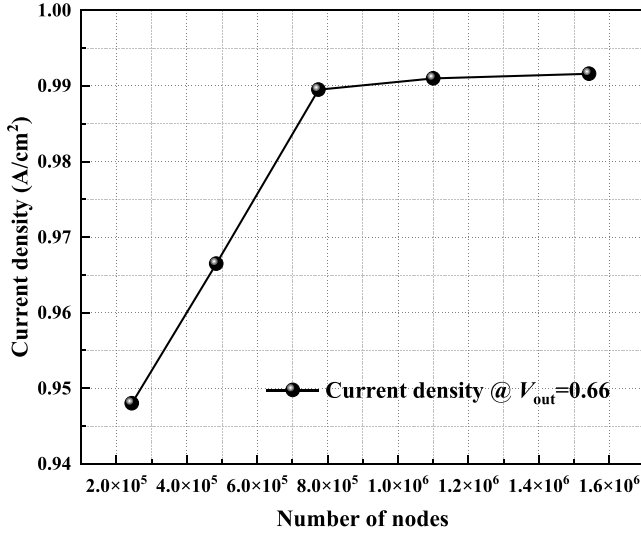
(a) Grid independence examination
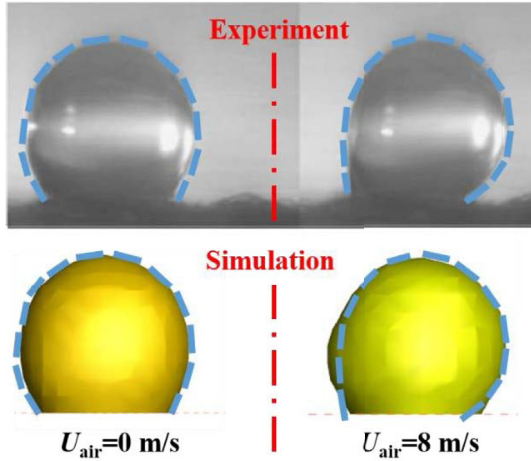
(b) VOF model
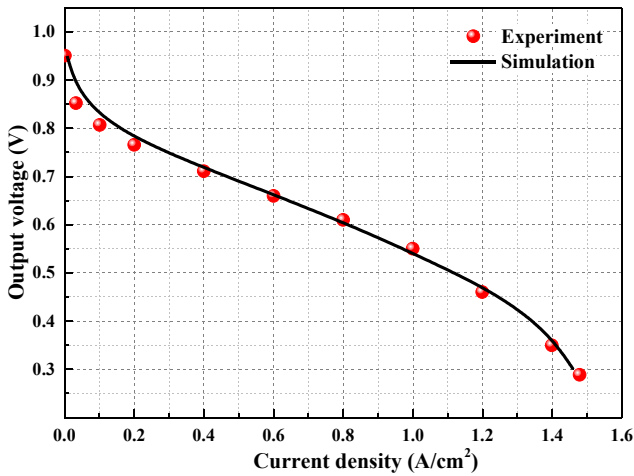
(c) 3D multiphase model

Fig. 6 – Model validation.

$$\nabla \cdot \left(\left(\rho C_p \overrightarrow{u} \right)^{\text{eff}} T \right) = \nabla \cdot \left(k^{\text{eff}} \nabla T \right) + S_E \tag{8}$$

where ρ_g, $\overrightarrow{u}_g$, Y_i, ϕ_{ele}, ϕ_{ion}, p_{lq}, λ_{mw}, and T denote the gas density, gas mixture velocity vector, mass fraction of species i, electronic potential, proton potential, liquid pressure, membrane water content, and temperature, respectively. In the momentum conservation equation, the porosity ε and permeability K (in source term) are two important parameters characterizing porous electrodes. The effective gas diffusion coefficient $D_i^{\text{eff}}$ (in Eq. (3)), electronic conductivity $\kappa_{\text{ele}}^{\text{eff}}$ (in Eq. (4)), and proton conductivity $\kappa_{\text{ion}}^{\text{eff}}$ (in Eq. (5)) take into consideration porosity and liquid water. And the effective thermal conductivity k^{eff} (in Eq. (8)) considers both fluid and solid thermal conductivity. The source terms in the governing equations used in the model are listed in Table 3. The expressions of the essential model parameters are given in Table 4 and Ref [59].

Boundary condition
For the fuel and air inlet, the mass fluxes (kg/(m²·s)) of gas mixtures are defined as

$$m_{flux,a} = \frac{\rho_a I \xi_a A_{act}}{2F c_{inlet,H_2} A_{a,in}} \tag{9}$$

$$m_{flux,c} = \frac{\rho_c I \xi_c A_{act}}{4F c_{inlet,O_2} A_{c,in}} \tag{10}$$

The molar concentrations of reactants are calculated by the inlet pressure $p_{a,in}$/ $p_{c,in}$, temperature $T_{a,in}$/ $T_{c,in}$ and relative humidity RH_a/ RH_c as follows:

$$c_{inlet,H_2} = \frac{p_{a,in} - RH_a p_{sat}}{RT_{a,in}} \tag{11}$$

$$c_{inlet,O_2} = \frac{0.21 \left(p_{c,in} - RH_c p_{sat} \right)}{RT_{c,in}} \tag{12}$$

The electronic potentials at the end of the anode and cathode BP surface are defined as

$$\phi_{\text{ele,a}} = 0 \tag{13}$$

$$\phi_{\text{ele,c}} = V_{out} \tag{14}$$

About temperature, the convection thermal boundary condition is specified at the anode and cathode end surface to simulate the effect of coolant, and other surrounding walls are fixed as operating temperature. Besides, the other boundary condition is defined as $\frac{\partial \phi_i}{\partial x_j} = 0$, where ϕ is the scalar to be solved, x_j is the normal direction of specific face.

The operating condition (temperature/pressure/stoichiometric ratio/relative humidity) used in our model is listed in Table 4. In Section 2.3.1, the solution subdoamins of different governing equations are indicated in the bracket following the title of the equation. Only the energy governing equations is solved in the whole solution domain. It should be noted that the interface between different layers (regions) (e.g., the interface between GDL and MPL in anode or cathode) is regarded as interior faces and no special treatment is needed for such inner face. The different layers own different physical

(a) Polorization curve

(b) Total power density

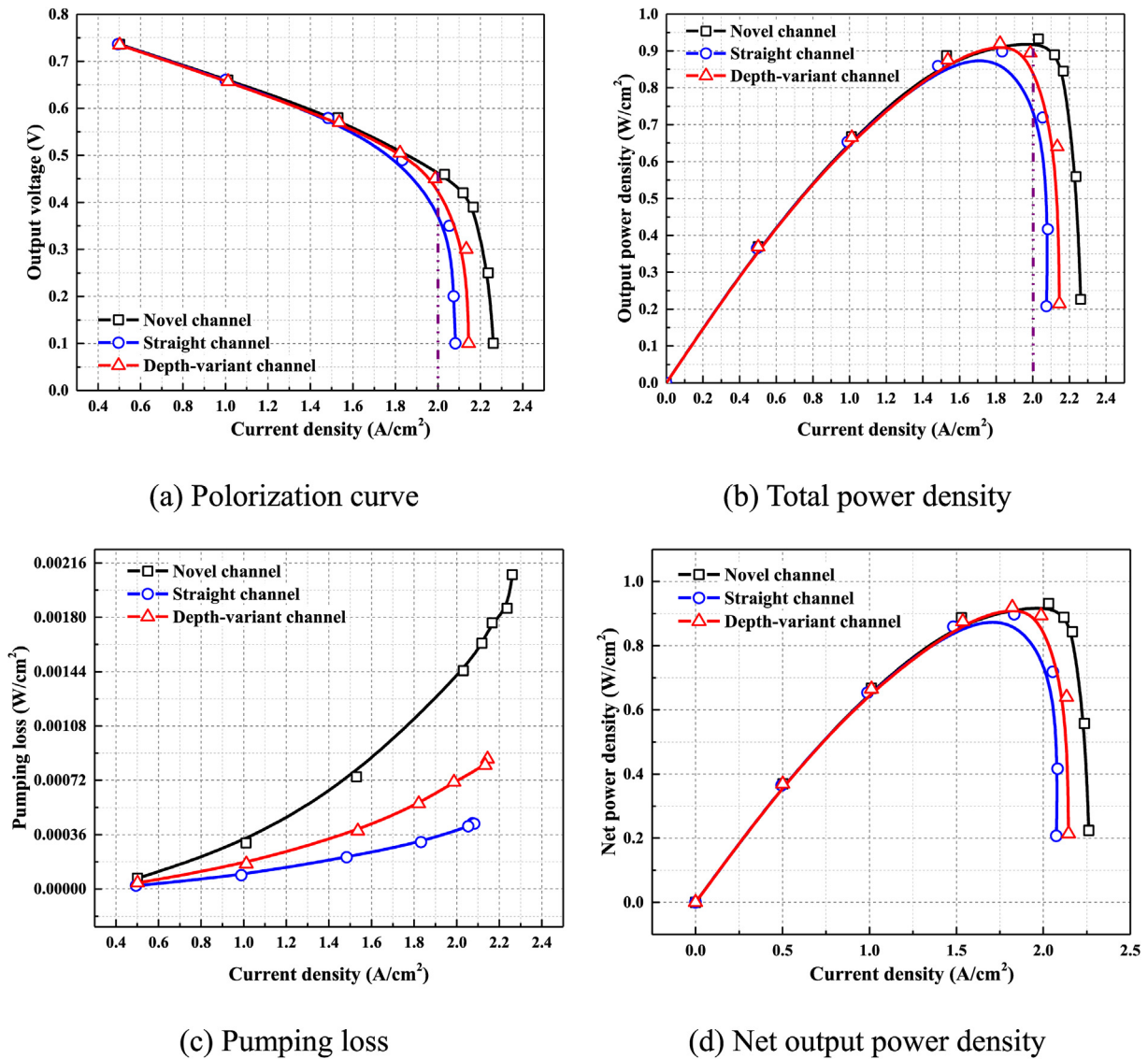

(c) Pumping loss

(d) Net output power density

Fig. 7 – Performance comparison of the different flow field.

properties and different source terms in the governing equations. Such numerical solution technique can guarantee the satisfaction of conservation condition in the solution domain while save computational time [61,62].

Water transport model

It is well-known that the liquid water produced in porous media would flow into the gas channel and discharge under the action of airflow purging. Ensuring the rapid discharge of water is of great significance in preventing PEMFC flooding and improving cell performance. Therefore, the VOF multiphase model is adopted to study the liquid water dynamic behavior in the gas channel [63]. In our novel flow field, the C-D part and straight part alternate periodically along the flow direction. Considering the time cost, these two parts are modeled respectively, named straight channel and C-D channel, as shown in Fig. 5. The water enters the channel from the fixed position on the GDL surface. Then it grows gradually,

leaves the water injection location, and moves to the channel outlet under the action of airflow. Model assumptions include.

(i) Due to the small Reynolds number, the flow is laminar and incompressible;
(ii) The phase change of liquid water is neglected;
(iii) The bottom wall of the channel represents the isotropic gas diffusion layer.

The governing equation and boundary conditions are shown below.

Governing equations
Mass conservation equation:

$$\frac{\partial \rho}{\partial t} + \nabla \cdot (\rho \vec{u}) = 0 \tag{15}$$

Momentum conservation equation:

(a) Contour of gas velocity in the straight channel

(b) Contour of gas velocity in the novel channel

(c) Contour of pressure in the straight channel

(d) Contour of pressure in the novel channel

(e) Pressure and velocity vector (only direction) in A-A'cross section of Fig.(d)
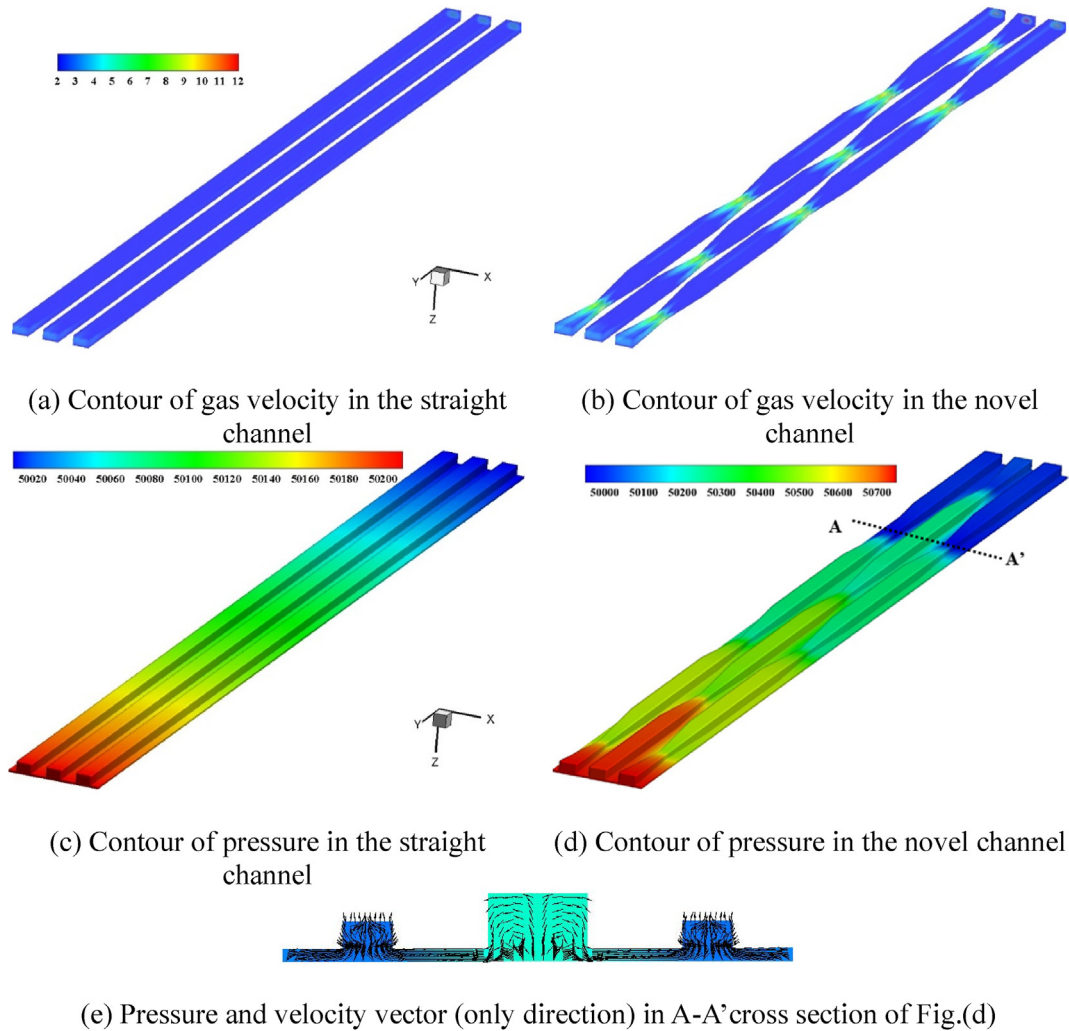
Fig. 8 – Gas velocity in the straight and different flow field.
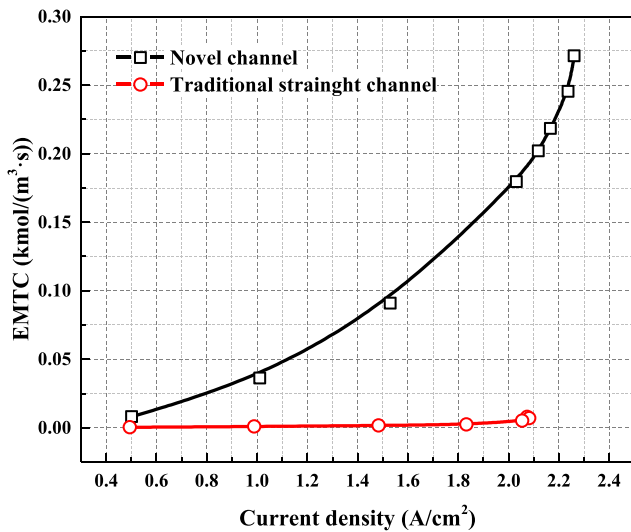
Fig. 9 – Effective mass transfer coefficient in novel and conventional flow field.

$$\frac{\partial(\rho \vec{u})}{\partial t} + \nabla \cdot (\rho \vec{u}\,\vec{u}) = -\nabla p + \nabla \cdot [\mu(\nabla \vec{u} + \nabla \vec{u}^{\mathrm{T}})] + \rho \vec{g} + \vec{F} \qquad (16)$$

The source term, F, in the momentum conservation equation, considers the surface tension force. Adopting the continuum surface force (CSF) model, $\vec{F}$ can be expressed as:

$$\vec{F} = 2\sigma k \frac{\rho \nabla C_l}{(\rho_1 + \rho_2)} \qquad (16a)$$

The mean curvature of the liquid/gas interface k is computed from the local gradient of the surface normal ∇C_l, as follows,

$$k = \nabla \cdot \left(\frac{\nabla C_l}{|\nabla C_l|} \right) \qquad (17)$$

Volume fraction conservation equation:

$$\frac{\partial(C_i \rho_i)}{\partial t} + \nabla \cdot \left(C_i \rho_i \vec{u}_i \right) = 0 \qquad (18)$$

where C_i is the volume fraction of species i, C_g represents the gas phase, and C_l represents the liquid phase. And $C_g + C_l = 1$.

(a) O$_2$ concentration in cathode   (b) O$_2$ concentration in cathode GDL-Novel
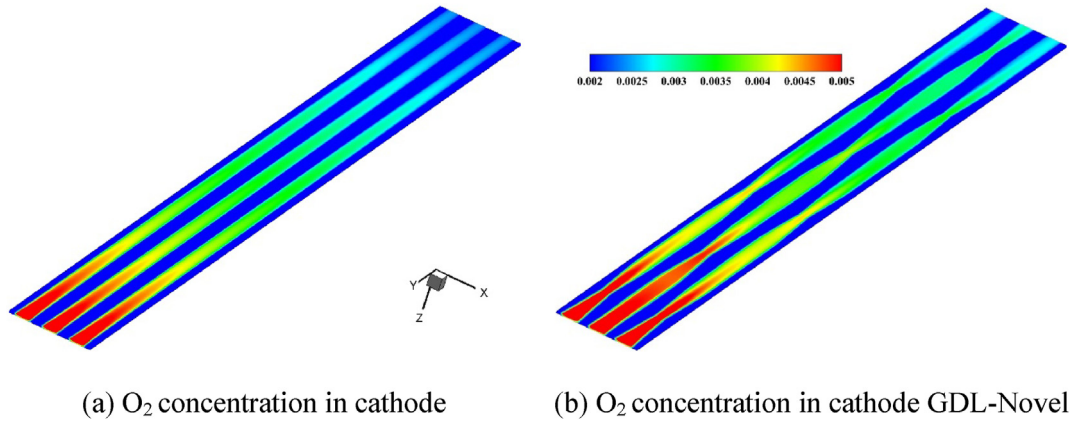
Fig. 10 — O$_2$ concentration in cathode GDL.

(a) Effect of the stoichiometric ratio

(b) Effect of operating pressure

(c) Promotion rate of stoichiometric ratio variation

(d) Promotion rate of pressure variation

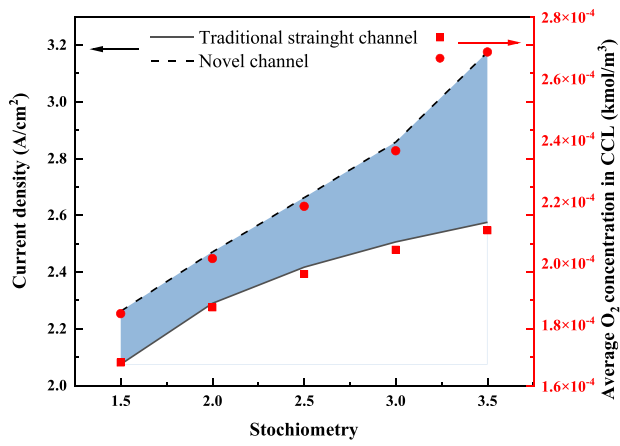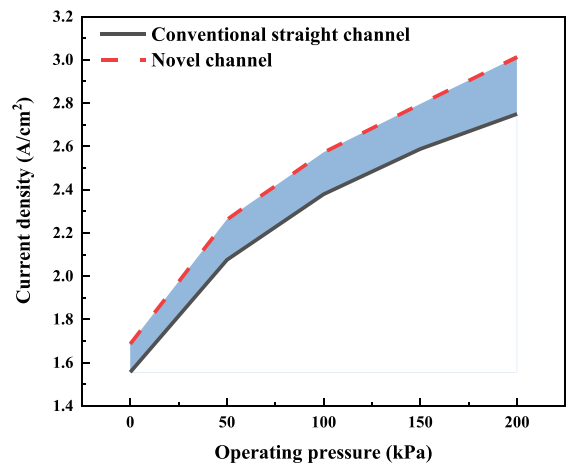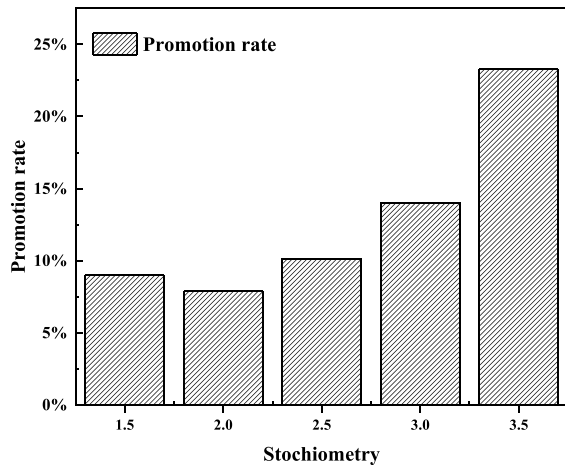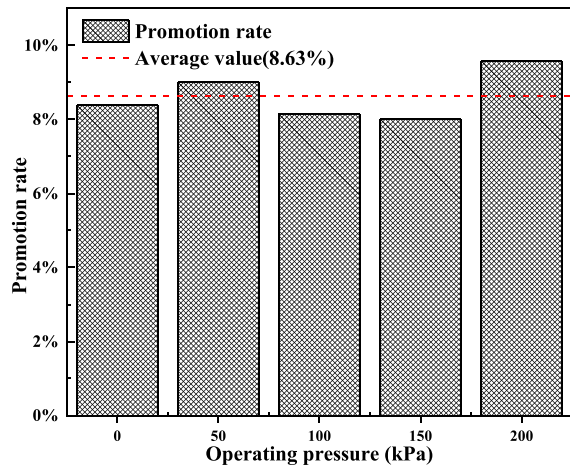**Fig. 11 — Effect of operating condition on performance.**

**Table 6 – Case setting to study the effect of geometry parameters.**

	h_1/h_2	w_1/w_2
Case 1	50%	30%
Case 2	50%	50%
Case 3	50%	70%
Case 4	30%	50%
Case 5	70%	50%

Boundary conditions

For the inlet condition, the inlet velocity of air and water is specified at the corresponding boundary, respectively. For the outlet condition, the outflow boundary condition is applied. The non-slip boundary condition is adopted at channel walls and GDL surface. For the contact angle, the wall of the channel is hydrophilic, and the GDL surface is hydrophobic. These values are listed in Table 5. The air inlet velocity is extracted at 2.0 A/cm^2 in the performance simulation.
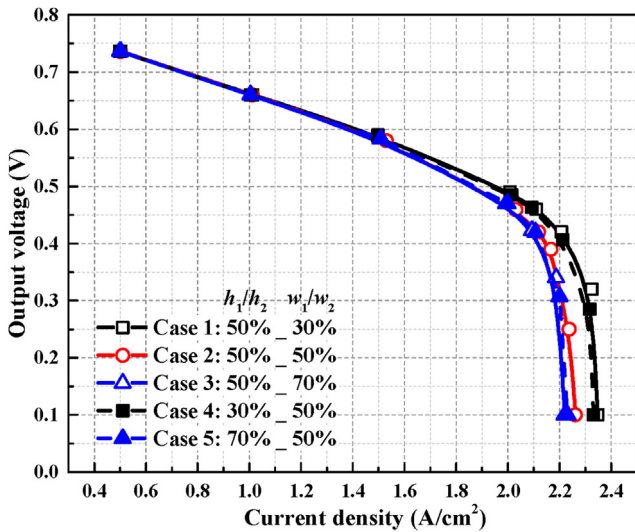
(a) V-I curve for novel flow field with different width and depth ratio
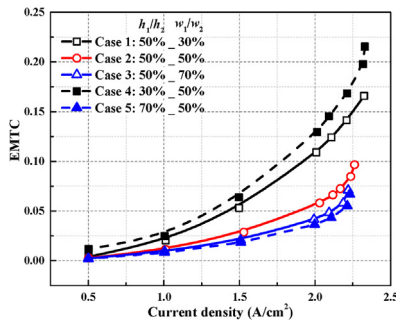
(b) EMTC for novel flow field with different width and depth ratio

Fig. 12 – Effect of geometry parameters.

Effective mass trasfer coeeficient

To compare the mass transfer ability of different flow fields, the effective mass transfer coefficient (EMTC) is adopted in the present study [28,29]. It is defined as follows,

$$e = \left| w \frac{\partial c}{\partial z} \right| \tag{19}$$

Here w is the velocity component in the through-plane direction (z direction). The effect of convection (w) and diffusion (concentration gradient) mass transfer are both considered in the expression. This indicator is proven to be applicable for the evaluation of the PEMFC performance with different flow fields [66].

Numerical procedure

All governing equations (both the two-fluid model and VOF model) stated above are solved by the finite volume method in the software ANSYS FLUENT. The user-defined functions (UDF) written by C code are implemented to update and customize source terms, transport properties, and boundary conditions during the solving process. The SIMPLE algorithm is adopted for coupling pressure and velocity. The V-cycle multigrid technique is employed to get substantial convergence. Residual with a magnitude of 1×10^{-6} is considered as convergence criteria for all equations. The mesh used to discrete the computing domain is shown in Figs. 2 and 3(c), which was determined after a grid-independent examination. The grid independence analysis is performed with five different grid numbers: 243,689, 484,005, 774,285, 1,101,739, and 1,542,885, as shown in Fig. 6(a). The current density change is smaller than 0.5% for the mesh with 1,101,739 nodes. Considering the accuracy, and computational cost, a grid number of 1.1 million is adopted here to perform the numerical simulation. The structured hexahedron mesh is adopted in the whole domain. In VOF transient simulation, a fixed time step of 5×10^{-7}s is employed to ensure the maximum Courant number is not exceeded [67]. Moreover, to verify the VOF model, the morphology of water droplets obtained by numerical simulation and experiment [68] at different air velocities is compared, as shown in Fig. 6(b). The difference is quite small, which proves the model is accurate. The numerical model used for validation has the same settings as the experiment. For example, the droplet diameter is 1 mm, and the calculation domain is 7 mm × 2.5 mm × 51 mm.

For the 3D multiphase model, the simulated polarization curve is compared with the test data in Ref. [69] under the same operating condition. As shown in Fig. 6(c), the predicted polarization curve is in good agreement with the experiment data, which validated our model accuracy.

Results and discussions

The cell performance improvement is analyzed in Section 3.1. Then the effect of operating conditions and geometry parameters on performance are investigated in Sections 3.2 and
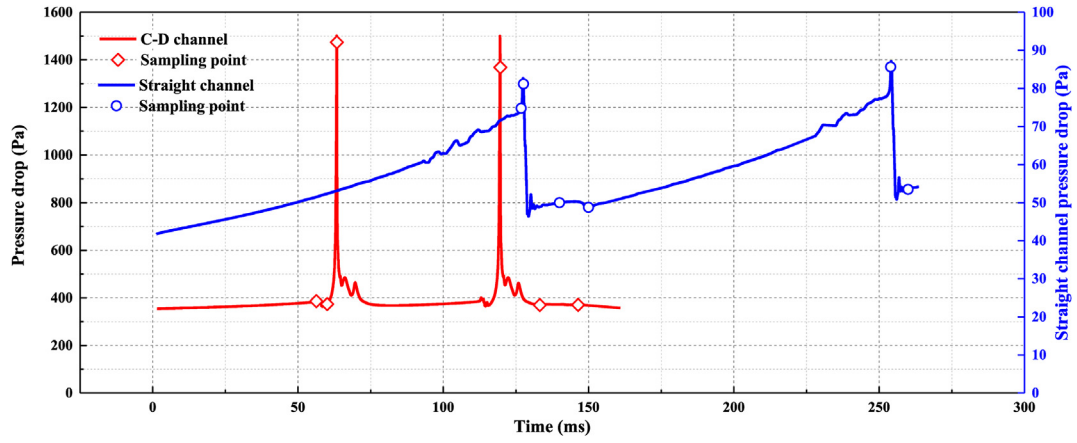
Fig. 13 − Pressure variation under different channel structures.
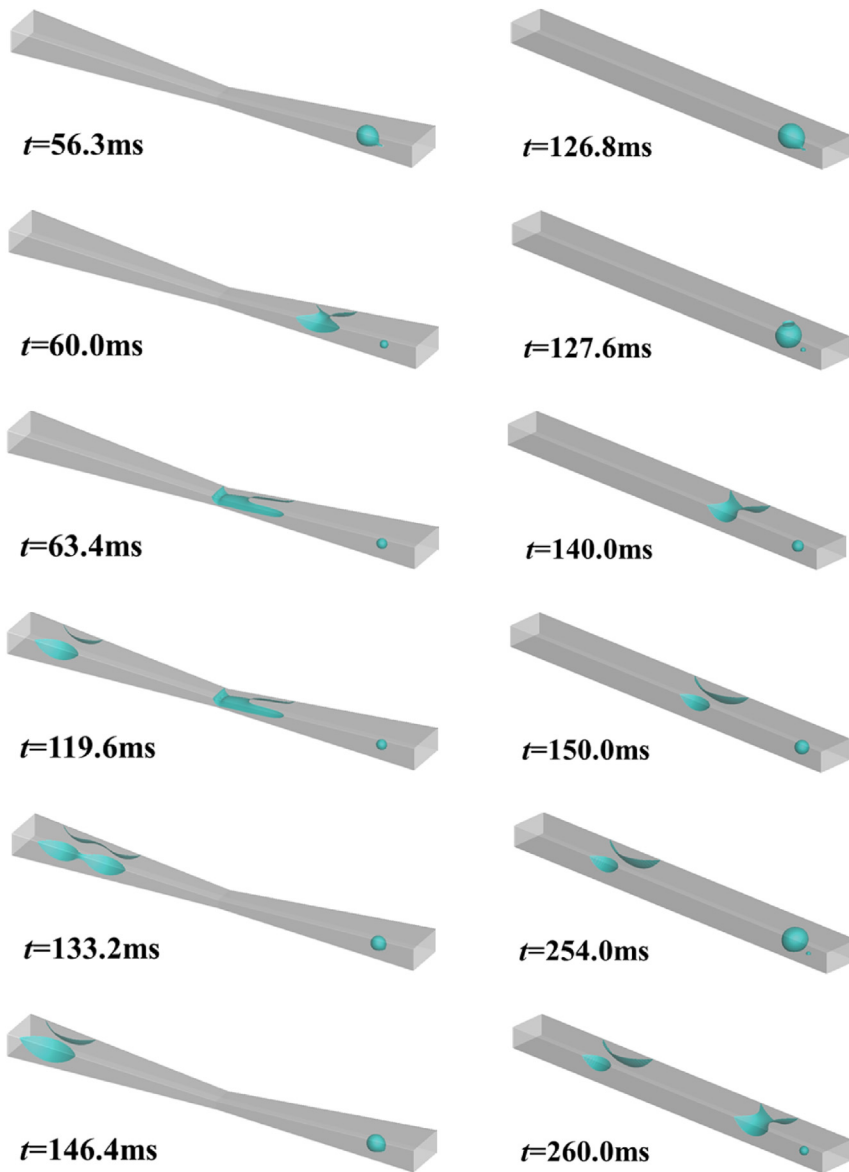

Fig. 14 − Water dynamic in channels.

3.3, respectively. Lastly, the drainage performance for novel and conventional channels is compared in Section 3.4.

Performance improvement

Output performance

Based on the validated 3D multiphase model, the cell performance is simulated with different cathode flow fields, as shown in Fig. 7. Compared with the depth-variant flow field, the novel flow field can further improve the performance, especially in the concentration polarization region. This indicates that channel with both width and depth variation outperforms a channel with only depth variation (e.g., 3D wave channel [30]). Under the same output current density of 2.0 A/cm^2, the output voltage or the total power density of novel and depth-variant flow field increase by about 25.2% and 14.2%, respectively.

After the C-D pattern is applied in the cathode flow field, the pump power in the cathode channel increases, as shown in Fig. 7(c). The pumping loss W$_{pump}$ is calculated by

$$W_{pump} = \frac{\Delta p q_v}{A_{act}\varsigma}$$

(20)

where $\varsigma = 0.7$ is the compressor efficiency [47].Although the pumping loss of the novel cathode flow field is higher than the conventional straight one, it is rather small (two orders of magnitudes lower) compared with the total output power density. As a result, the novel flow field still has advantage in net output power density, as shown in Fig. 7(d).

Under land cross flow

Under land cross flow in PEMFC, which is in favor of reactant transport, has been observed by many researchers [70,71]. The staggered arrangement of C-D in a novel flow field also induces the cross flow.

Fig. 8(a) and (b) represent the contour of gas velocity in the cathode flow field. The local high speed (about 7 m/s) can be observed near the C-D location in the novel flow field (Fig. 8(b)), while in the straight flow field, it maintains a relatively uniform low velocity (about 2 m/s) field (Fig. 8(a)). Furthermore, different flow characteristics cause different pressure distributions, as shown in Fig. 8(c) and (d). The pressure decreases monotonously from the channel inlet to the channel outlet in the straight flow field. The novel flow field presents a scale-like pressure distribution by contrast. That means there always exists a pressure difference between two adjacent flow channels along the flow direction.

As shown in Fig. 8(e), the A-A' cross-section is extracted and plotted the velocity vector on that. The pressure difference induces the under land cross flow through the gas diffusion layer, obviously. This convection flux is a benefit for reactant gas transport and liquid water drainage. In a straight channel, only the diffusion caused by concentration difference can cause the gas transport from the channel to the catalyst layer.

Mass transfer enhancement

The average effective mass transfer coefficient is calculated in the cathode channel, as shown in Fig. 9. The EMTC increases with the current density due to the increase in the inlet flow rate. The average EMTC in the novel cathode flow field is two orders of magnitude higher than that in the conventional flow field. As a result, the O$_2$ concentration in GDL is higher in the novel flow field case, as shown in Fig. 10. The violent velocity disturbance (Fig. 8(e)) is the main reason that promotes mass transfer.

Effect of operating condition on the limited current density

To study the effect of operating conditions (operating pressure and cathode stoichiometric ratio) on cell performance, the current density is simulated under the same output voltage (V$_{out}$ = 0.1V). Under this output voltage, the cell works in the concentration loss zone. It's worthy to note that as long as the cell work in the concentration loss area, the qualitative results here are still valid and instructive.

From Fig. 11(a), it can be observed that the performance of both novel and conventional flow field increases with the stoichiometric ratio. In the conventional case, the growth rate gradually slowed down, but the novel case is the opposite. In other words, the superiority of the novel flow field becomes more obvious under a high flow rate. This could be explained by the reactant concentration. Different from that under the same current density, in the present study, the simulation is under the same output voltage. The more O$_2$ concentration, the higher the reaction rate. As shown in the right coordinate axis in Fig. 11(a), with the enhanced mass transfer, the average O$_2$ concentration in CCL is higher for the novel flow field case. And the concentration of both the new flow field and the traditional flow field increases with the increase of the stoichiometric ratio. This leads to a higher reaction rate and therefore a higher current density. The blue-filled area in Fig. 11(a) represents the performance improvement of the novel flow field. It is obvious that with the increase of the stoichiometric ratio, the promotion rate also generally increases, as shown in Fig. 11(c).

For the effect of operating pressure, increasing the operating pressure represents the increase of reactant concentration. As a result, the performance improved. With the increase of operating pressure, the growth rate of both two flow fields' current densities gradually slows down, as shown in Fig. 11(b). From Fig. 11(d), the current density of the novel flow field is 8.63% higher than the conventional case on average. Different from the effect of the stoichiometric ratio, the promotion rate is not particularly sensitive to the operating pressure.

Effect of geometry parameters

In a novel flow field, the dimension of the C-D part has an influence on the performance. To explore the effects of width and depth shrinkage five cases are set up, as listed in Table 6. Fig. 12(a) shows the polarization curve with different width ratios and depth ratios. For the effect of width ratio (Case 1/2/3), it can be observed that the novel flow field with a smaller width ratio possesses a better performance, especially under a high current density zone. As illustrated in Fig. 12(b), the novel flow field with 30% width ratio could own the biggest EMTC value. The smaller the width ratio, the higher the EMTC,

which means better mass transfer ability. As a result, under the concentration zone, where the cell performance is limited mainly by the reactant concentration, adequate oxygen could be supplied to the catalyst surface. For the effect of depth (Case 2/4/5), the smaller the depth, the better the performance. Compared with the width ratio, the effect of the depth ratio on mass transfer is more significant, as shown in Fig. 12(b). That is because the depth variation of the channel directly increases the gas through-plane velocity toward the porous layer, which causes a higher EMTC value. In a word, for the C-D part in the novel flow field, a narrower structure is more conducive to mass transfer.

Liquid water transport behavior

Fig. 13 shows the time evolution of the pressure drop in two kinds of channel parts during drainage. Fig. 14 shows the location and shape of the droplet in two parts. The corresponding time points of Fig. 14 are annotated in Fig. 13.

As the droplets grow, the pressure drop increases gradually. The pressure force and viscous force constitute the driving force of droplet movement. When the driving force is higher than the wall adhesion force, the droplet detachment happens and moves forward downstream, as shown in time $t = 56.3$ ms (Fig. 14). During the process of the droplet moving forward, the gas-liquid interface will contact the top surface of the channel. Due to the hydrophilic character of the wall, under the effect of wall adhesion and surface tension force, the spherical droplet deforms and moves upwards and adsorbs to the top surface of the channel, as shown in time $t = 60.0$ ms (Fig. 14). The liquid droplets leave the surface of GDL, which is conducive to the reaction gas entering the pores of GDL from the flow channel. Then the droplet gradually becomes a liquid film ($t = 63.4$ ms in Fig. 14) when moving to the narrow region, under the increasing driven force. And the pressure drop peak occurs. The increasing viscous force (due to the increase of velocity) and pressure force are both conducive to droplet discharge. Similarly, at $t = 119.6$ ms (Fig. 14), the second droplet moves to the narrow region and causes the second pressure drop peak in Fig. 13. After that, the rear droplets catch up ($t = 133.2$ ms in Fig. 14) with the front droplets and merge into one($t = 146.4$ ms in Fig. 14).

For straight channels, the droplet doesn't detach the water inlet orifice until 126.8 ms (t=126.8 ms in Fig. 14), and the first pressure drop peak in Fig. 13 is also near this time point. A bigger droplet detachment size is observed compared to the C-D part channel. This is caused by the small driving force in the straight channel. The lower velocity and pressure drop leads to lower shear viscous force and pressure force, respectively. After leaving the water inlet orifice, the droplet may deform during movement and contact with the top surface of the channel, as shown at $t = 127.6$ ms (Fig. 14). Then, same as the behavior in the C-D structure case, the droplet moves upwards under the effect of hydrophilic wall adhesion force. Different from the C-D case, during moving at the top surface of the channel (for example, $t = 140.0$ ms and $t = 150.0$ ms in Fig. 14), the droplet remains spherical with a certain curvature without pulling and spreading. At $t = 254.0$ ms, the second

droplet is ready to detach and the second pressure drop peak (Fig. 14) occurs. Then it repeats the same behavior with the first droplet until discharge out of the channel (take t=260.0 ms, for example).

Comparing the droplet dynamic behavior in these two different parts, at t=146.4 ms, the droplet in the C-D structure has moved near the outlet. However, for the straight case at $t = 150$ ms, the droplet has only moved to a position half of the distance away from the inlet. Therefore, it can be concluded that the import of the C-D structure will greatly enhance the drainage capacity of the flow field.

Conclusion

In this work, a novel flow field that can promote mass transfer and improve cell performance is proposed. The 3D multiphase model is adopted to simulate the output performance, and the VOF method is used to study droplet dynamic behavior in the novel channel. The main findings of this study are as follows.

(1) The total power density of the novel flow field is improved by about 25.2% under the same output current density of 2.0 A/cm^2. After subtracting the pumping loss, the net total power density is still greatly improved.

(2) The novel flow field could enhance the under land cross flow and leads to a higher effective mass transfer coefficient (EMTC). This is beneficial to the reactant transport under the concentration difference dominant zone.

(3) The promotion rate is not particularly sensitive to the operating pressure but increases with the increase of the stoichiometric ratio.

(4) For the C-D part in the novel flow field, a narrower structure (by changing the width ratio and depth ratio) is more conducive to mass transfer and boosting performance.

(5) The novel flow field owns a better drainage capacity; however, the movement of droplets to the C-D section will cause a sharp increase in pressure.

Declaration of competing interest

The authors declare that they have no known competing financial interests or personal relationships that could have appeared to influence the work reported in this paper.

Acknowledgement

REFERENCES

[1] Mu Y-T, He P, Bai F, Chen L, Qu Z-G, Tao W-Q. Numerical analyses on oxygen transport resistances in polymer electrolyte membrane fuel cells using a novel agglomerate model. Int J Hydrogen Energy 2023;48:3232–51.

[2] Wang Y, Ruiz Diaz DF, Chen KS, Wang Z, Adroher XC. Materials, technological status, and fundamentals of PEM fuel cells – a review. Mater Today 2020;32:178–203.

[3] Zhang Z, Wang Q-Y, Bai F, Chen L, Tao W-Q. Performance simulation and key parameters in-plane distribution analysis of a commercial-size PEMFC. Energy 2023;263:125897.

[4] Zhang Z, He P, Dai Y-J, Jin P-H, Tao W-Q. Study of the mechanical behavior of paper-type GDL in PEMFC based on microstructure morphology. Int J Hydrogen Energy 2020;45(53):29379–94.

[5] Xu Z, Qiu D, Yi P, Peng L, Lai X. Towards mass applications: a review on the challenges and developments in metallic bipolar plates for PEMFC. Prog Nat Sci: Mater Int 2020;30(6):815–24.

[6] Shaigan N, Yuan X-Z, Girard F, Fatih K, Robertson M. Standardized testing framework for quality control of fuel cell bipolar plates. J Power Sources 2021;482:228972.

[7] Porstmann S, Wannemacher T, Drossel WG. A comprehensive comparison of state-of-the-art manufacturing methods for fuel cell bipolar plates including anticipated future industry trends. J Manuf Process 2020;60:366–83.

[8] Leng Y, Ming P, Yang D, Zhang C. Stainless steel bipolar plates for proton exchange membrane fuel cells: materials, flow channel design and forming processes. J Power Sources 2020;451:227783.

[9] Iwan A, Malinowski M, Pasciak G. Polymer fuel cell components modified by graphene: electrodes, electrolytes and bipolar plates. Renew Sustain Energy Rev 2015;49:954–67.

[10] Antunes RA, de Oliveira MCL, Ett G, Ett V. Carbon materials in composite bipolar plates for polymer electrolyte membrane fuel cells: a review of the main challenges to improve electrical performance. J Power Sources 2011;196(6):2945–61.

[11] Wilberforce T, El Hassan Z, Ogungbemi E, Ijaodola O, Khatib FN, Durrant A, et al. A comprehensive study of the effect of bipolar plate (BP) geometry design on the performance of proton exchange membrane (PEM) fuel cells. Renew Sustain Energy Rev 2019;111:236–60.

[12] Marappan M, Palaniswamy K, Velumani T, Chul KB, Velayutham R, Shivakumar P, et al. Performance studies of proton exchange membrane fuel cells with different flow field designs - review. Chem Rec 2021;21(4):663–714.

[13] Kahraman H, Orhan MF. Flow field bipolar plates in a proton exchange membrane fuel cell: analysis & modeling. Energy Convers Manag 2017;133:363–84.

[14] Xu C, Zhao TS. A new flow field design for polymer electrolyte-based fuel cells. Electrochem Commun 2007;9(3):497–503.

[15] Zhang L, Shi Z. Optimization of serpentine flow field in proton-exchange membrane fuel cell under the effects of external factors. Alex Eng J 2021;60(1):421–33.

[16] Min C, He J, Wang K, Xie L, Yang X. A comprehensive analysis of secondary flow effects on the performance of PEMFCs with modified serpentine flow fields. Energy Convers Manag 2019;180:1217–24.

[17] Xu X, Yang W, Zhuang X, Xu B. Experimental and numerical investigation on effects of cathode flow field configurations in an air-breathing high-temperature PEMFC. Int J Hydrogen Energy 2019;44(45):25010–20.

[18] Shimpalee S, Greenway S, Van Zee JW. The impact of channel path length on PEMFC flow-field design. J Power Sources 2006;160(1):398–406.

[19] Limjeerajarus N, Santiprasertkul T. Novel hybrid serpentine-interdigitated flow field with multi-inlets and outlets of gas flow channels for PEFC applications. Int J Hydrogen Energy 2020;45(25):13601–11.

[20] Hazar H, Yilmaz M, Sevinc H. A comparative analysis of a novel flow field pattern with different channel size configurations. Fuel 2022;319:123867.

[21] Zhang Y, He S, Jiang X, Ye Y, Xiong M, Yang X. Characteristics of proton exchange membrane fuel cell considering "dot matrix" gas distribution zones and waveform staggered flow field with cooling channels. Energy Convers Manag 2022;267:115881.

[22] Rahmani E, Moradi T, Ghandehariun S, Naterer GF, Ranjbar A. Enhanced mass transfer and water discharge in a proton exchange membrane fuel cell with a raccoon channel flow field. Energy 2023;264:126115.

[23] Iranzo A, Arredondo CH, Kannan AM, Rosa F. Biomimetic flow fields for proton exchange membrane fuel cells: a review of design trends. Energy 2020;190:116435.

[24] Sauermoser M, Pollet BG, Kizilova N, Kjelstrup S. Scaling factors for channel width variations in tree-like flow field patterns for polymer electrolyte membrane fuel cells - an experimental study. Int J Hydrogen Energy 2021;46(37):19554–68.

[25] Kahraman H, Coban A. Performance improvement of a single PEM fuel cell using an innovative flow field design methodology. Arabian J Sci Eng 2020;45(7):5143–52.

[26] Trogadas P, Cho JIS, Neville TP, Marquis J, Wu B, Brett DJL, et al. A lung-inspired approach to scalable and robust fuel cell design. Energy Environ Sci 2018;11(1):136–43.

[27] Yoshida T, Kojima K. Toyota MIRAI fuel cell vehicle and progress toward a future hydrogen society. J Electrochem Soc 2015;24:45–9.

[28] Cai Y, Fang Z, Chen B, Yang T, Tu Z. Numerical study on a novel 3D cathode flow field and evaluation criteria for the PEM fuel cell design. Energy 2018;161:28–37.

[29] Shen J, Tu Z, Chan SH. Performance enhancement in a proton exchange membrane fuel cell with a novel 3D flow field. Appl Therm Eng 2020;164:114464.

[30] Chen X, Yu Z, Yang C, Chen Y, Jin C, Ding Y, et al. Performance investigation on a novel 3D wave flow channel design for PEMFC. Int J Hydrogen Energy 2020;46:11127–39.

[31] Yan X, Guan C, Zhang Y, Jiang K, Wei G, Cheng X, et al. Flow field design with 3D geometry for proton exchange membrane fuel cells. Appl Therm Eng 2019;147:1107–14.

[32] Zhang G, Qu Z, Tao WQ, Wang X, Wu L, Wu S, et al. Porous flow field for next-generation proton exchange membrane fuel cells: materials, characterization, design, and challenges. Chem Rev 2022;123:989–1039.

[33] Wan Z, Yan H, Sun Y, Yang C, Chen X, Kong X, et al. Thermal management improvement of air-cooled proton exchange membrane fuel cell by using metal foam flow field. Appl Energy 2023:333.

[34] Zhang G, Bao Z, Xie B, Wang Y, Jiao K. Three-dimensional multi-phase simulation of PEM fuel cell considering the full morphology of metal foam flow field. Int J Hydrogen Energy 2020;46:2978–89.

[35] Bao Z, Wang Y, Jiao K. Liquid droplet detachment and dispersion in metal foam flow field of polymer electrolyte membrane fuel cell. J Power Sources 2020;480:229150.

[36] Bao Z, Niu Z, Jiao K. Gas distribution and droplet removal of metal foam flow field for proton exchange membrane fuel cells. Appl Energy 2020;280:116011.

[37] Azarafza A, Ismail MS, Rezakazemi M, Pourkashanian M. Comparative study of conventional and unconventional designs of cathode flow fields in PEM fuel cell. Renew Sustain Energy Rev 2019;116:109420.

[38] Zuo Q, Li Q, Chen W, Peng R, Zhu X, Xie Y, et al. Optimization of blocked flow field performance of proton exchange membrane fuel cell with auxiliary channels. Int J Hydrogen Energy 2022;47:39943–60.

[39] Perng S-W, Wu H-W, Wang R-H. Effect of modified flow field on non-isothermal transport characteristics and cell performance of a PEMFC. Energy Convers Manag 2014;80:87–96.

[40] Wang B, Chen W, Pan F, Wu S, Zhang G, Park JW, et al. A dot matrix and sloping baffle cathode flow field of proton exchange membrane fuel cell. J Power Sources 2019;434:226741.

[41] Niu Z, Fan L, Bao Z, Jiao K. Numerical investigation of innovative 3D cathode flow channel in proton exchange membrane fuel cell. Int J Energy Res 2018;42(10):3328–38.

[42] Fan L, Niu Z, Zhang G, Jiao K. Optimization design of the cathode flow channel for proton exchange membrane fuel cells. Energy Convers Manag 2018;171:1813–21.

[43] Heidary H, Kermani MJ, Advani SG, Prasad AK. Experimental investigation of in-line and staggered blockages in parallel flowfield channels of PEM fuel cells. Int J Hydrogen Energy 2016;41(16):6885–93.

[44] Guo H, Chen H, Ye F, Ma CF. Baffle shape effects on mass transfer and power loss of proton exchange membrane fuel cells with different baffled flow channels. Int J Energy Res 2019;43(7):2737–55.

[45] Ghanbarian A, Kermani MJ. Enhancement of PEM fuel cell performance by flow channel indentation. Energy Convers Manag 2016;110:356–66.

[46] Cai Y, Wu D, Sun J, Chen B. The effect of cathode channel blockages on the enhanced mass transfer and performance of PEMFC. Energy 2021;222:119951.

[47] Zhang G, Xie B, Bao Z, Niu Z, Jiao K. Multi-phase simulation of proton exchange membrane fuel cell with 3D fine mesh flow field. Int J Energy Res 2018;42(15):4697–709.

[48] Zehtabiyan-Rezaie N, Arefian A, Kermani MJ, Noughabi AK, Abdollahzadeh M. Effect of flow field with converging and diverging channels on proton exchange membrane fuel cell performance. Energy Convers Manag 2017;152:31–44.

[49] Havaej P. A numerical investigation of the performance of Polymer Electrolyte Membrane fuel cell with the converging-diverging flow field using two-phase flow modeling. Energy 2019;182:656–72.

[50] Timurkutluk B, Chowdhury MZ. Numerical investigation of convergent and divergent parallel flow fields for PEMFCs. Fuel Cell 2018;18(4):441–8.

[51] Wang X-D, Huang Y-X, Cheng C-H, Jang J-Y, Lee D-J, Yan W-M, et al. An inverse geometry design problem for optimization of single serpentine flow field of PEM fuel cell. Int J Hydrogen Energy 2010;35(9):4247–57.

[52] Song J, Guo H, Ye F, Ma CF. Mass transfer and cell performance of a unitized regenerative fuel cell with nonuniform depth channel in oxygen-side flow field. Int J Energy Res 2019;43(7):2940–62.

[53] Ramin F, Sadeghifar H, Torkavannejad A. Flow field plates with trap-shape channels to enhance power density of polymer electrolyte membrane fuel cells. Int J Heat Mass Tran 2019;129:1151–60.

[54] Zhang Y, He S, Jiang X, Xiong M, Ye Y, Yang X. Three-dimensional multi-phase simulation of different flow fields with cooling channel in proton exchange membrane fuel cell. Int J Hydrogen Energy 2022;47:37929–44.

[55] Yin C, Song Y, Liu M, Gao Y, Li K, Qiao Z, et al. Investigation of proton exchange membrane fuel cell stack with inversely phased wavy flow field design. Appl Energy 2022;305:117893.

[56] Hamrang A, Abdollahzadeh M, Bilondi AM, Bagherighajari F, Rahgoshay SM, Pascoa JC. Comparison of PEMFC performance with parallel serpentine and parallel serpentine-baffled flow fields under various operating and geometrical conditions; a parametric study. Int J Hydrogen Energy 2022;48:7442–59.

[57] Hu K, Zhao P, Wang S, Wang Y. Three-dimensional multiphase simulation of a partially narrowed flow field configuration for a high-performance polymer electrolyte membrane fuel cell. Appl Therm Eng 2023;223:119986.

[58] Park D, Ham S, Sohn Y-J, Choi Y-Y, Kim M. Mass transfer characteristics according to flow field and gas diffusion layer of a PEMFC metallic bipolar plate for stationary applications. Int J Hydrogen Energy 2023;48:304–17.

[59] He P, Mu Y-T, Park JW, Tao W-Q. Modeling of the effects of cathode catalyst layer design parameters on performance of polymer electrolyte membrane fuel cell. Appl Energy 2020;277:115555.

[60] Zhang G, Wu L, Qin Z, Wu J, Xi F, Mou G, et al. A comprehensive three-dimensional model coupling channel multi-phase flow and electrochemical reactions in proton exchange membrane fuel cell. Advances in Applied Energy 2021;2.

[61] Patankar SV. Numerical heat transfer and fluid flow. New York: McGraw-Hill; 1980.

[62] Tao WQ. Numerical heat transfer. 2nd ed. Xi'an: Xi'an JiaotongUniversity; 2001.

[63] Hirt CW, Nichols BD. Volume of fluid (VOF) method for the dynamics of free boundaries. J Comput Phys 1981;39(1):201–25.

[64] Zhu X, Sui PC, Djilali N. Dynamic behaviour of liquid water emerging from a GDL pore into a PEMFC gas flow channel. J Power Sources 2007;172(1):287–95.

[65] Chen L, He Y-L, Tao W-Q. Effects of surface microstructures of gas diffusion layer on water droplet dynamic behaviors in a micro gas channel of proton exchange membrane fuel cells. Int J Heat Mass Tran 2013;60:252–62.

[66] Shen J, Tu Z, Chan SH. Evaluation criterion of different flow field patterns in a proton exchange membrane fuel cell. Energy Convers Manag 2020;213:112841.

[67] Anyanwu IS, Larry AO, Liu Z, Jiao K. Water transport in GDL microstructures of nonuniform fiber diameter arrangement. J Energy Eng 2022;148. 06022001.

[68] Theodorakakos A, Ous T, Gavaises M, Nouri JM, Nikolopoulos N, Yanagihara H. Dynamics of water droplets detached from porous surfaces of relevance to PEM fuel cells. J Colloid Interface Sci 2006;300:673–87.

[69] Ozen DN, Timurkutluk B, Altinisik K. Effects of operation temperature and reactant gas humidity levels on performance of PEM fuel cells. Renew Sustain Energy Rev 2016;59:1298–306.

[70] Taira H, Liu H. In-situ measurements of GDL effective permeability and under-land cross-flow in a PEM fuel cell. Int J Hydrogen Energy 2012;37(18):13725–30.

[71] Bachman J, Santamaria A, Tang H-Y, Park JW. Investigation of polymer electrolyte membrane fuel cell parallel flow field with induced cross flow. J Power Sources 2012;198:143–8.